Energies **2014**, *7*, 5675-5700; doi:10.3390/en7095675

OPEN ACCESS

energies

ISSN 1996-1073

www.mdpi.com/journal/energies

Article

An Acausal Li-Ion Battery Pack Model for Automotive Applications

Kotub Uddin [1,*], Alessandro Picarelli [2], Christopher Lyness [3], Nigel Taylor [3] and James Marco [1]

[1] WMG, International Digital Laboratory, the University of Warwick, Coventry CV4 7AL, UK; E-Mail: james.marco@warwick.ac.uk

[2] Claytex Services Ltd., Edmund House, Rugby Road, Leamington Spa CV32 6EL, UK; E-Mail: alessandro.picarelli@claytex.com

[3] Hybrids & Electrification, Jaguar & Land Rover, Banbury Road, Warwick CV35 0XJ, UK; E-Mails: clyness@jaguarlandrover.com (C.L.); ntaylo15@jaguarlandrover.com (N.T.)

* Author to whom correspondence should be addressed; E-Mail: k.uddin@warwick.ac.uk; Tel.: +44-2476-151-322.

Received: 24 July 2014; in revised form: 13 August 2014 / Accepted: 19 August 2014 / Published: 28 August 2014

Abstract: In this work, a novel acausal and reconfigurable battery pack model is presented. The model structure adopted for the battery cell is based on an equivalent circuit representation. The circuit elements are modified to take account of both hysteresis and diffusion limitation. The latter is known to be a nonlinear function of large operating currents or long operating times. It is shown that the integration of a current dependent time constant within the cell model better emulates the solid diffusional dynamics of lithium intercalation into the active material under large electrical loads. The advantages of an acausal modeling approach, when scaling-up individual cell models into a complete battery system are also presented. Particular consideration is given to emulating the impact of cell to cell variations on pack performance. Using statistical analysis of battery tests, cell model parameter variations are characterized and quantified. The cell and scaled-up pack model are parameterized for a number of commercially available cell formats, energy capacities and chemistries. The new models are validated using transient, real-world, electrical data measured from an electric vehicle (EV) operating within an urban environment.

Keywords: lithium ion; battery modeling; electric vehicle (EV); battery management system; battery pack

---

1. Introduction

A key enabler, or constraint, of the electrified power train is the need to store energy in a form that can be easily and efficiently converted into electricity. In recent years, electrochemical batteries have emerged as the preferred technology for in-vehicle energy storage. However, despite considerable increases in energy density and power capability [1], many vehicle manufacturers and system integrators still believe that the technology demands many compromises to be made by the customer. For example, the phenomenon of range-anxiety is widely reported within a number of studies including [2–4]. Many of the technology challenges and commercial opportunities associated with the integration of battery systems within the next generation of electric vehicles (EVs) are underpinned by the inherent properties of the Li-ion cell.

The need to accurately, rapidly and robustly model both the performance of individual cells and their aggregated performance when scaled-up into a complete system is of paramount importance to vehicle manufacturers [5]. Within this context, computer simulation is widely employed to facilitate concept evaluation, vehicle and system prototyping, and the virtual verification of different EV and hybrid EV (HEV) architectures and technology options [6]. Modelling methods provide a framework to translate observations into physical phenomena and thus better understand the complexities of the electrochemical system under a wide variety of operating and environmental conditions. The challenge for energy storage system engineers, electrochemical engineers and material scientists is to optimise the trade-off between model accuracy and model fidelity (in terms of the data and computational requirements needed to construct and execute the models).

Porous electrode theory, pioneered by Fuller *et al.* [7] provides the benchmark modeling framework for electrochemical battery simulation and is widely reported within the literature. The model solves the one-dimensional (1-D) problem for lithium diffusion dynamics and charge transfer kinetics that predicts the electrical response of the cell within a paired intercalation electrode system. Extensions to porous electrode theory have focused on improving our understanding of the dynamics of non-ideal active materials [8–11], charge transfer kinetics [10,12] and the structural characterization of electrode microstructures [13]. The development of high fidelity single cell models is of immense value to the scientific community investigating novel cell designs and innovations in material science. However, due to their complexity and computational burden, they are arguably of less value for system level analysis and the management of automotive energy storage systems. In recent years, several simplifications to these models have been published in an attempt to improve their run-time performance associated with resolving solid phase diffusion [14]. A combination of perturbation techniques, volume averaging, and intuition-based simplifications was adopted to achieve real-time simulation [15], however, to derive the lower-order model through this method requires extensive pre-processing and a-priori knowledge of system behaviors under varying conditions which is not easily realizable. Other techniques employed to derive reduced-order models for lithium-ion batteries include: Chebyshev polynomial methods [16], Galerkin's method [17], residue grouping methods [18] and Proper Orthogonal Decomposition methods [19]. While these models significantly reduce the computational resources required for model execution and the simulation results from individual cells correlate well with the results of higher fidelity models and experimental data [19], their complexity, computational burden

and the need for physical data for parameterization still remains an impediment for scaling-up individual cell models to a complete battery system model.

A number of recent publications advocate the use of equivalent circuit models (ECMs) as the most appropriate trade-off between electrochemical models and, at the other end of the spectrum, simply modeling the battery as an empirical function. Parameterization of the cell model typically employs standard test methods such as electrochemical impedance spectroscopy (EIS) and high power pulse characterization (HPPC) [20]. This approach is limited by the difficulty in unambiguously interpreting the circuit elements. However, ECMs do provide a degree of understanding as to the internal cell mechanisms and causalities for different frequency regions and hence the ability to correlate the simulation output with measureable parameters such as open circuit voltage (V_{oc}) and steady-state resistance.

ECMs have previously been used to study complete battery systems [21,22] but have either ignored the non-linear response of the cells to large currents (*i.e.*, diffusion limitation) or the effects of cell-to-cell variations when up-scaling individual cell models to complete battery system models. It is argued that including cell-to-cell variations within the system model can only be efficiently studied through an acausal modeling approach [23–25]. In this work, we present the development of an acausal battery simulation tool that accounts for all these properties. We extend a, proven ECM for Li-ion cells [26] (described in Section 2) to include temperature dependence, voltage hysteresis, self-discharge and diffusion limitation. Furthermore, instead of using the traditional input-output simulation structure [27] we adopt an acausal approach in which mathematical relations in the model are defined at model compilation and can therefore adapt to varying battery system architectures. A detailed discussion retaining to acausal simulation is beyond the scope of the this paper, further information is provided in [28,29].

This paper is structured as follows: Section 2 defines the ECM representation of the Li-ion cell in which current dependency is included within the model's parameterization strategy; Section 3 discusses the design of the complete battery pack model in which key cell-to-cell variations within the parameterization of the pack model are included; Implementation of the model follows an acausal simulation strategy; validation of the model at both the cell and system level is presented using real-world data recorded from an EV operating within an urban environment; discussion, further work and concluding remarks are presented in Sections 4 and 5, respectively.

2. Cell Model Development

2.1. Cell Model Structure

2.1.1. Cell Electrical Model

Modeling the electronic and thermal behavior of a battery cell requires the characterization of mechanisms across multiple time constants and the definition of parameters that are dynamically coupled. The ECM adopted here, is presented within Figure 1 and extends research previously published within [26]. The lumped-parameter model structure comprises a parallel resistor-capacitor (RC) network connected in series with a capacitor, a resistor and an ideal voltage source. The internal resistances includes the Ohmic resistance R_0 which comprises all electronic resistances and the

polarization resistance R_d which when coupled with C_d accounts for ion diffusion [25,30]. The equivalent capacitance C_{Th} accounts for the variation in V_{oc} with the time integral of load current [20].

Figure 1. Equivalent circuit model (ECM) structure of an individual cell.

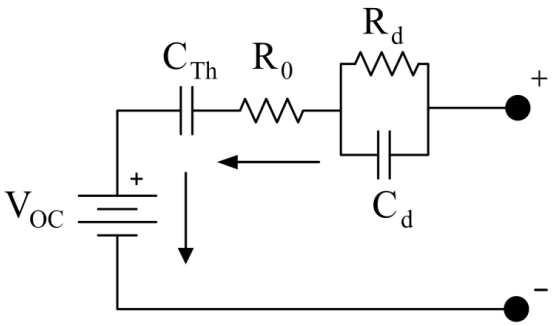

The original ECM structure, without modification, does not include parameter dependency on temperature and state of charge (*SOC*). Furthermore, the non-linear current dependency of the circuit components or the effects of self-discharge or hysteresis when defining the cell's V_{oc} are not included. When the ECM is implemented using an acausal approach, each component depicted in Figure 1 separately satisfies a suitable governing equation in a context-independent form. The interaction between the components is formalized in terms of their connections without any definition of causality (*i.e.*, no variable is declared a-priori as input or output). This declarative modelling strategy is fundamentally different from a procedural or causal approach where the model is formalized in terms of model inputs and outputs. The outcomes of an equation based or "declarative" modeling approach is acausal which, as discussed in [29], results in a higher level of re-usability in addition to improved model readability. The global electrical behavior of the ECM is described by the set of differential and algebraic equations:

$$V_L = V_{oc} - I_L R_0 - U_{Th} - U_d \tag{1}$$

$$\frac{d}{dt}U_d + \frac{U_d}{R_d C_d} = \frac{I_L}{C_d} \tag{2}$$

$$\frac{d}{dt}U_{Th} = I_L \frac{dV_{OC}}{dQ_{Th}} \tag{3}$$

where V_L denotes the terminal voltage; I_L denotes the load current; U_{Th} denotes the voltage drop across the capacitor C_{Th}; U_d is voltage drop due to polarization effects; and Q_{Th} is the accumulated charge within the cell. The coupled set of Equations (1)–(3) can be solved analytically and without loss of generality, with a solution given by:

$$V_L = V_{oc} - I_L R_0 - \frac{1}{C_{Th}}\int I_L dt - \frac{e^{-\frac{t}{R_d C_d}}}{C_d}\int e^{\frac{t}{R_d C_d}} I_L dt \tag{4}$$

Equation (4) has five unknown parameters (V_{oc}, R_0, C_{Th}, C_d and R_d). When compared to electrochemical models (which may have in excess of 88 parameters that must be defined [31]) the attraction of the ECM approach to cell modeling is further reinforced. This is particularly the case when the cell model is embedded within an optimization algorithm, such as within management systems to predict runtimes and dynamic power estimations [32–34]. Within the context of EV

performance simulation [25], introducing further RC terms within the model will increase the computational effort required without offering a discernable improvement in model accuracy.

The parameters of the ECM shown in Figure 1 (V_{oc}, R_0, C_{Th}, C_d and R_d) are defined as variables that depend on temperature, current and *SOC*. The *SOC* is defined using the well understood column counting equation:

$$SOC = SOC(t_0) - \frac{100}{Q_{\text{rated}}}\int_{t_0}^{t_f} I_L \cdot dt \quad (5)$$

where Q_{rated} is the rated capacity of the cell and therefore defines the total amount of charge that can be reversibly cycled from the cell.

V_{oc} hysteresis that results from thermodynamic entropic effects, mechanical stress, and microscopic distortions within the active electrode materials [35] can be critical for reliable state estimation. This is particularly the case for lithium iron phosphate (LFP) cells which are known to exhibit very little variation in V_{oc} for the entire *SOC* range of the cell. The hysteresis contributions V_h to the cell's V_{oc} is accounted by redefining the definition of V_{oc}:

$$V_{oc} = U_{oc} + V_h \quad (6)$$

where U_{oc} is the mean open circuit potential extracted from charging and discharging galvanostatic intermittent titration technique (GITT) experiments. The hysteresis voltage (V_h) is defined by the first-order differential equation:

$$\frac{dV_h}{dt} = -\frac{1}{\beta} I_L \left[V_{h,max} + \text{sign}(I_L) V_h\right] \quad (7)$$

where β defines a constant derived through experimentation and $V_{h,max}$ is the limiting hysteresis voltage. Equation (7) is constructed such that for prolonged as well as large pulse charge currents the hysteresis voltage tends to $V_{h,max}$. Conversely for prolonged as well as large pulse discharge currents the hysteresis voltage will tend to $-V_{h,max}$. A graphical representation of Equation (7) is presented Figure 2.

Figure 2. Illustrating the characteristics of Equation (7), for large current magnitudes and pulse times the hysteresis voltage tends to a maximum deviation of $V_{h,max}$.

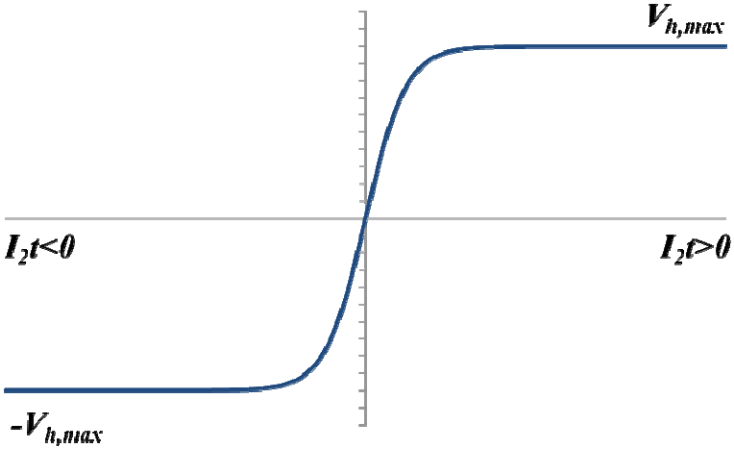

The *RC* component shown in Figure 1 contributes a time constant $\tau = R_d C_d$ to the bulk diffusion process of Li-ions within the solid phase. While electrolyte and solid phase diffusion both influence

the low-frequency voltage response the relative significance of electrolyte concentration gradients are found to be small. In this work therefore, we neglect the contribution arising from liquid phase diffusion which would otherwise introduce additional time constants (RC-pairs) into Equation (4).

The dynamics of the cell voltage are driven by contributions from the ohmic, kinetic and mass transport polarizations. The ohmic contribution is independent of current magnitude and pulse length, while as suggested by the Tafel equation [36] the kinetic polarization decreases with current magnitude. The mass transfer polarization (represented by the pre-exponential terms in the Butler-Volmer equation [36]) increases as a function of both current magnitude and pulse duration. This mass transport polarization is thought to be dominated by diffusion within the solid state [37]. As larger currents are applied to the cell, the dynamics of ions in the solid phase more quickly enter a regime of diffusion limitation where the surface concentration of lithium may be significantly different than the average concentration contained within the active material. The average concentration indicates the concentration level that would be reached if the current were interrupted and the cell was allowed to reach equilibrium. This is noteworthy since the diffusivity of ions, *i.e.*, the time constant of overvoltage, will therefore depend on the applied current. In our work we therefore assume a generic polynomial form for the time constant ($\tau(I_L)$) to take account of the non-linear voltage response to large current pulses.

2.1.2. Cell Thermal Model

A common assumption employed within the literature is to assume that temperature is homogenous across the entire surface of the cell. This assumption is convenient, since it facilitates a significant simplification of the resulting thermal governing equations.

However, as highlighted in Figure 3, the assumption is not valid for Li-ion pouch cells. Figure 3 shows the surface temperature variation measured using a thermal imaging camera when a 20-A·h $LiFePO_4$ pouch cell and a 20-A·h $LiNiCoMnO_2$ pouch cell experience a 2C electrical load. The figure illustrates that an appreciable temperature gradient can develop within some cells. In the case of the $LiFePO_4$ cell a surface temperature differential of 2.7 °C was recorded by the thermocouples while a 3 °C difference was measured for the $LiNiCoMnO_2$ cell. Similar results have been reported in [38,39] that discuss the thermal performance of alternative cell chemistries and form-factors. In this work our primary aim is to study the electrical behavior of complete battery packs. As a result, we define a cell "effective operating temperature".

The "effective operating temperature" is similar to the prescription proposed by [40] for dealing with thermal gradients within lithium battery performance models. The authors studied cells with significant temperature gradients and found that they exhibit lower impedance than that expected from the theoretical average temperature. Temperature gradients were treated by calculating an effective temperature for the cell by first discretising the cell into resistive elements connected in parallel followed by summing the temperature dependent resistances to calculate an effective resistance and finally, using Equations (8)–(10) calculating the effective temperature.

Figure 3. Surface temperature map attained using thermal imaging camera of: (**left**) a 20-A·h $LiFePO_4$ pouch cell; and (**right**) a 20-A·h $LiNiCoMnO_2$ pouch cell under a 2C load.

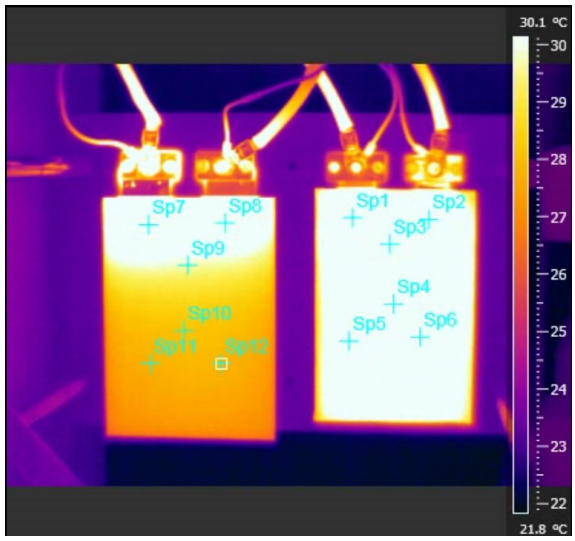

For a single cell, if we assume a closed system where there are no mass flows, *i.e.*, heat transfers, we can assume:

$$mC_p\Delta T = Q \tag{8}$$

where m is the mass of the cell; C_p is the specific heat capacity; T is the effective temperature; and Q is the heat generated. The heat flow $\dot{Q}$ is given by [41]:

$$\dot{Q} = I\left(V - V_{oc} - T_{ref}\frac{dV_{oc}}{dT}\right) \tag{9}$$

where $I(V - V_{oc})$ represents irreversible joule heating caused by Li-ion transport. The differential term within Equation (9) represents the reversible rate of heat generation due to entropy change within the cell. This model assumes no specific geometry for a single cell beyond a total volume with uniform temperature for some arbitrary body. Heat conduction between cells is assumed to be a linear function:

$$\dot{Q} = G\Delta T \tag{10}$$

For a pouch cell with a thermal conductivity k, area A and thickness L, the conductance G can be calculated as:

$$G = kA/L \tag{11}$$

It is noteworthy that the reversible entropic contribution to heat generation within Equation (9) may be important. This can intuitively be understood by considering that for electrochemical reactions under fixed pressure conditions the equilibrium potential is given by:

$$\frac{dV_{OC}}{dT} \cong \frac{\Delta S}{F} \tag{12}$$

where the ratio of entropy change ΔS (which, as suggested by Figure 4, can take values in the order of 40 at $SOC < 10\%$) to the Faraday constant F (96,487 C/mol) is in the order of 4×10^{-4}. This means the term $T_{ref}\frac{dV_{oc}}{dT}$ (which will be of the order 10^{-1}) in Equation (9) is comparable with the term $V - V_{oc}$ and should therefore not be neglected at small SOC values.

Figure 4. Discharge entropy change calculated using Equation (12) across state of charge (*SOC*) range for a 20-A·h $LiFePO_4$ pouch cell (dotted line), a 40-A·h $LiNiCoO_2$ pouch cell (solid line) and a 20-A·h $LiMn_2O_4$ cell (dashed line).

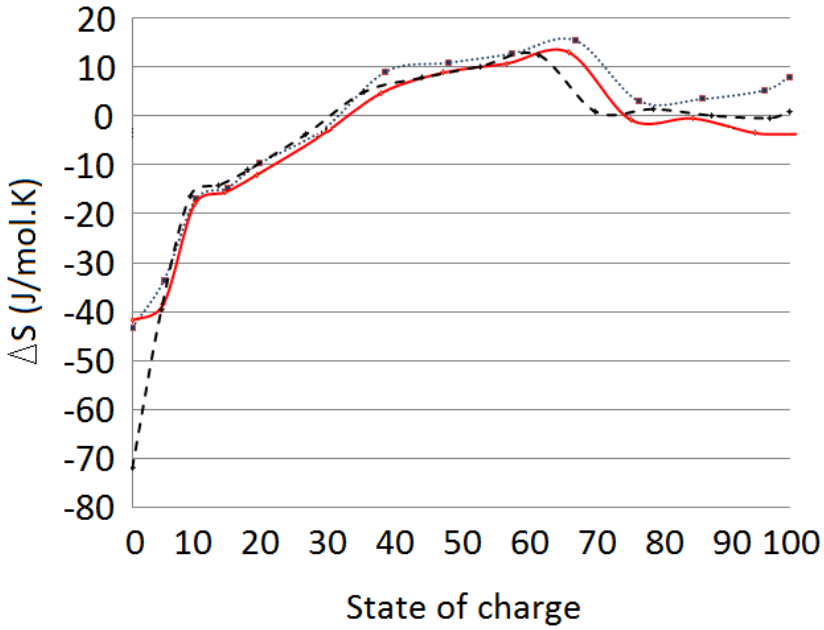

2.2. Cell Model Parameterization

2.2.1. Cell Electrical Model

The parameters of the ECM: V_{oc}, R_0, C_{Th}, C_d and R_d are calculated by fitting HPPC data—a series of 10-s charge and discharge pulses at different *SOC* values and temperatures—to Equation (4). To do this, we first re-write Equation (4) in a closed form [26]:

$$V_{L,i} = V_{oc,i} - I_{L,i}R_{0,i} - \frac{1}{C_{Th}}\sum_{i=0}^{n} I_{L,i}\Delta t_i - I_{d,i}R_{d,i} \quad (13)$$

$$I_{d,i} = \left[1 - \frac{1 - \exp\left(-\frac{\Delta t_i}{\tau_d}\right)}{\frac{\Delta t_i}{\tau_d}}\right] I_{L,i} + \left[1 - \frac{1 - \exp\left(-\frac{\Delta t_i}{\tau_d}\right)}{\frac{\Delta t}{\tau_d}} - \exp\left(-\frac{\Delta t_i}{\tau_d}\right)\right] I_{d,i} + \exp\left(-\frac{\Delta t_i}{\tau_d}\right) I_{d,i-1} \quad (14)$$

where the subindex i indicates the i^{th} time-step. Equations (13) and (14) are then written in matrix form:

$$\begin{pmatrix} V_{L,1} \\ V_{L,2} \\ \vdots \\ \vdots \\ V_{L,n} \end{pmatrix} = \begin{pmatrix} 1 & I_{L,1} & Ah_{L,1} & I_{d,1} \\ 1 & I_{L,2} & Ah_{L,2} & I_{d,2} \\ \vdots & \vdots & \vdots & \vdots \\ \vdots & \vdots & \vdots & \vdots \\ 1 & I_{L,n} & Ah_{L,n} & I_{d,n} \end{pmatrix} \begin{pmatrix} V_{oc} \\ R_0 \\ C_{Th}{}^{-1} \\ R_d \end{pmatrix} \quad (15)$$

where:

$$Ah_{L,i} = \sum_{k=1}^{i} I_{L,k}\Delta t \quad (16)$$

Employing data from a single pulse of the HPPC experiment corresponding to a single temperature, *SOC* and Current, we can completely determine the left hand side as well as the first matrix on the right hand side of Equation (15). Using linear least squares fitting we can then determine the time constant $\tau = R_d C_d$ minimizes the square error between predicted and measured voltage (HPPC test) and the corresponding values for V_{oc}, R_0, C_{Th} and R_d.

Given that a single HPPC test pulse—and hence the subsequent set of fitted parameters—is related to a single temperature, *SOC* and current, an algorithm is employed to repeat the process for all the combinations of T = −20 °C, 0 °C, 25 °C, 45 °C, *SOC* = 5%, 20%, 50%, 80%, 95% and $I_L = \frac{1}{5}I_{max}, \frac{2}{5}I_{max}, \frac{3}{5}I_{max}, \frac{4}{5}I_{max}, I_{max}$ which represents a typical operating envelope for EVs. It is important to include in the HPPC tests physical conditions that are close to the boundary of operation where batteries display non-linear behavior. For example, in lithium batteries possessing a graphite negative electrode there is highly non-linear V_{oc} dependency on *SOC* around very large and very small *SOC* values due changes in intercalation and de-intercalation phases [42,43] so it is important to include 5% and 95% *SOC* points in the characterization tests.

In Figure 5, we show a three dimensional plot of Ohmic resistance for a 30-A·h lithium nickel-manganese-cobalt oxide (NMC) cell as a function of *SOC* and discharge current for various ambient temperatures derived by fitting Equation (15) with experimental data. The effect of current magnitude on Ohmic resistance is dominated by internal temperature effects since larger currents only act, in this context, to raising internal temperature which departs rapidly from the ambient soak temperature. Similarly, pulse data is used to generate $V_{oc}(SOC, T)$, $R_d(SOC, I_L, T)$ as well as values for the other model parameters.

Figure 5. Internal resistance for a 30-A·h lithium nickel-manganese-cobalt oxide (NMC) cell as a function of temperature and *SOC* for various currents.

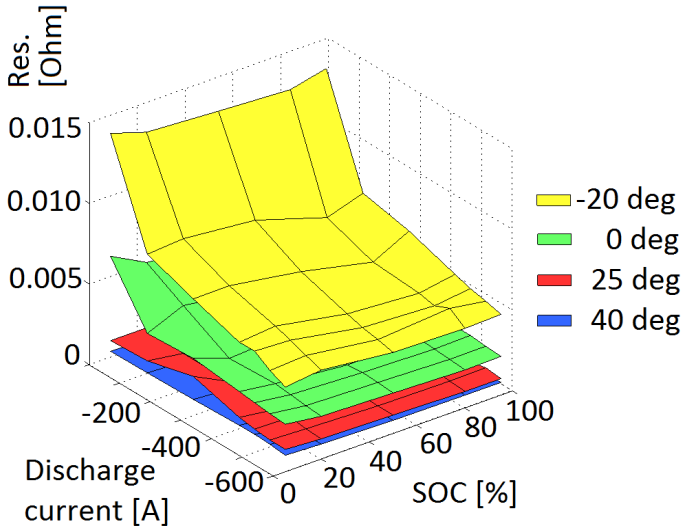

We have parameterized our model for a number of commercially available cells ranging a number of cell formats, sizes and chemistries including cells with LFP, manganese spinel (LMO), lithium nickel-cobalt-aluminium oxide (NCA), lithium cobalt oxide (LCO), NMC and mixed oxide cathode materials and graphite and lithium titanate (LTO) anode materials. We find cells with the same chemical compositions have similar $V_{oc}(SOC)$ profiles; however, internal resistance—which is

influenced by factors such as electronic contact between active electrode materials and current collectors, homogeneity of the active material paste, the battery internal structure—and polarization resistance—influenced by electrolyte composition—are found to differ. It can thus be established that both design as well as the manufacturing process itself will have a bearing on battery performance characteristics.

2.2.2. Cell Thermal Model

For each cell under evaluation, the heat capacity is calculated using a bespoke calorimeter. Values of 880 J/(kg·K) for 18,650 cells to 1900 J/(kg·K) for pouch cells are observed [44]. Thermal conductance is calculated either by appropriately summing the conductance of constituent material values taken from literature [42] or by curve fitting Equation (10) with simple bespoke experiments and high fidelity computational fluid dynamics (CFD) models.

2.3. Cell Model Implementation

Given model parameter values at fixed T, SOC and I_L a mechanism for interpolation that generates mathematically smooth estimates for the parameters such that $y = f(SOC, I_L, T)$ is required. Common practice within the literature is to employ a polynomial fitting function within the simulation. However, a known limitation of this approach is that the resulting function may not fit the data well [45]. In this work we utilize spline functions to generate smooth estimates for $y(SOC, T)$ which avoids oscillations within interpolated values either side of outliers [27]. Implementation of the model employs cubic splines because with the first-degree splines the slope of the spline may change abruptly at the data breakpoints. Conversely, for the second-degree splines, there is a discontinuity within the second derivative which means that the curvature of the quadratic spline changes abruptly at each node. The cubic spline function is defined in the x interval $[x_0, x_f]$ such that it is a polynomial of degree at most three on each subinterval and is continuous up to its second derivative. In our work, spline interpolation is coupled with linear interpolation where there is a weak correspondence between a model variable [46] and the model output.

Figures 6 and 7 present a subset of the validation results for the derived electro-thermal cell model. While the model has been validated for a number of commercially available cells, here we present results for a 30 A·h NMC pouch cell (Figure 6) and a 20 A·h LFP pouch cell (Figures 7a and 8c). The cells were cycled and monitored using a Bitrode Battery Cell Cycler with a ±5 mV and ±100 mA measurement error.

The NMC pouch cell was loaded with a 500 s drive cycle that accurately emulates a high performance EV around the Nürburgring racing track (Figure 6a); current pulses ranged between 11C discharge and 1C charge rates with fast transient dynamics. The transient discrepancy between measured and predicted voltages (shown in Figure 6b) is less than 50 mV. For the 20-A·h LFP cells, a 600 s artificial cycle shown in Figure 7a that contains 400 A (20C) discharge pulses were employed to validate the predication capabilities of the model. This aggressive cycle was chosen specifically to validate the model at the boundaries of the parameterization dataset, where cell performance is known to be more non-linear [37]. These results of the electro-thermal model are presented in Figure 7,

along with laboratory test data. Once again there is a maximum of 50 mV transient error between the measured and predicted voltages.

Figure 6. (**a**) Current profile used to test the 30 A·h NMC pouch cell; and (**b**) a comparison of predicted cycle voltage using the cell model (blue line) with actual test data (red line) for the 30 A·h NMC cell.

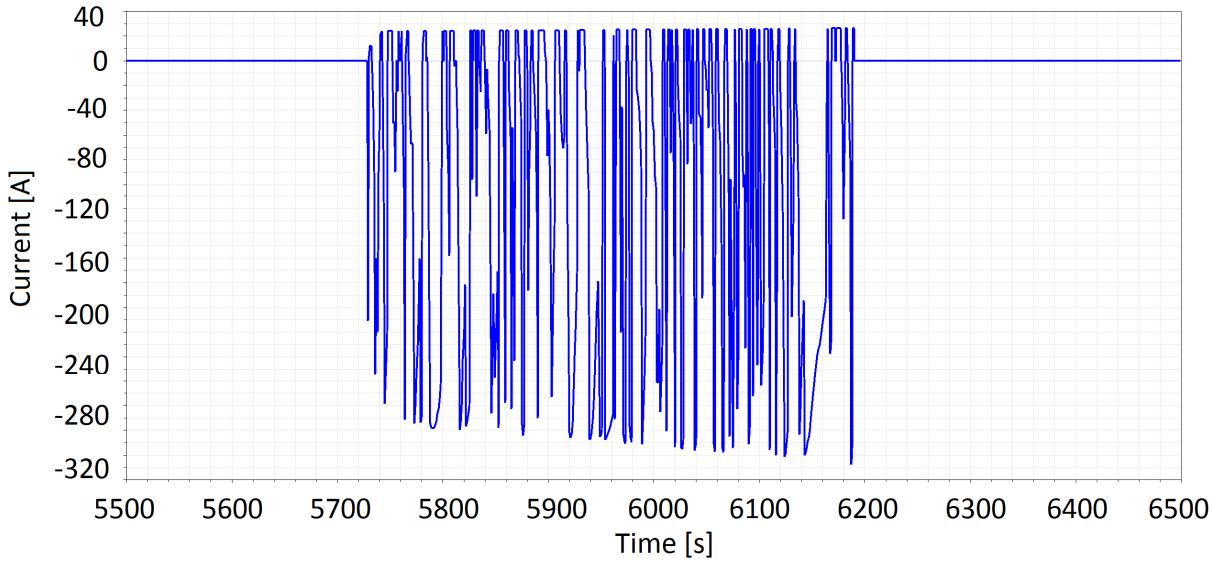

(**a**)

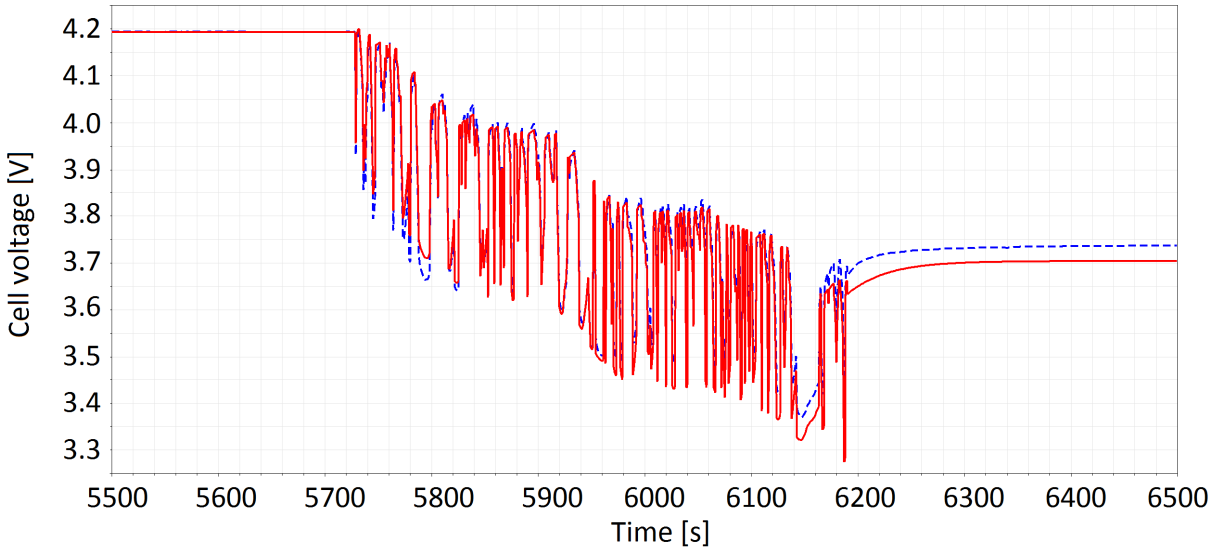

(**b**)

When parameterising and validating the performance of the cell model for different commercially available cell technologies, a peak error of approximately 45–75 mV was found to be persistent when comparing experimental data and the simulation output. This value is known to exceed the measurement tolerances of the experimental facilities employed and is deemed indicative of the phenomenological approach presented here. The authors acknowledge that the proposed electro-thermal model cannot completely describe the behavior of the electrochemical system. The simulation error is indicative of a physical effect that is unrepresented within the model, which the authors attribute to not codifying the cycling history of the cell within the model.

Figure 7. (**a**) Depicts a highly demanding current profile used for this validation process. The duration of this cycle is 600 s (excluding rest time) and the pulses range between 20C discharge and 10C charge; and (**b**) a comparison of predicted terminal voltage using the cell model (blue line) with actual test data (red line) for a 20 A·h lithium iron phosphate (LFP) cell. The maximum transient error is less than 50 mV.

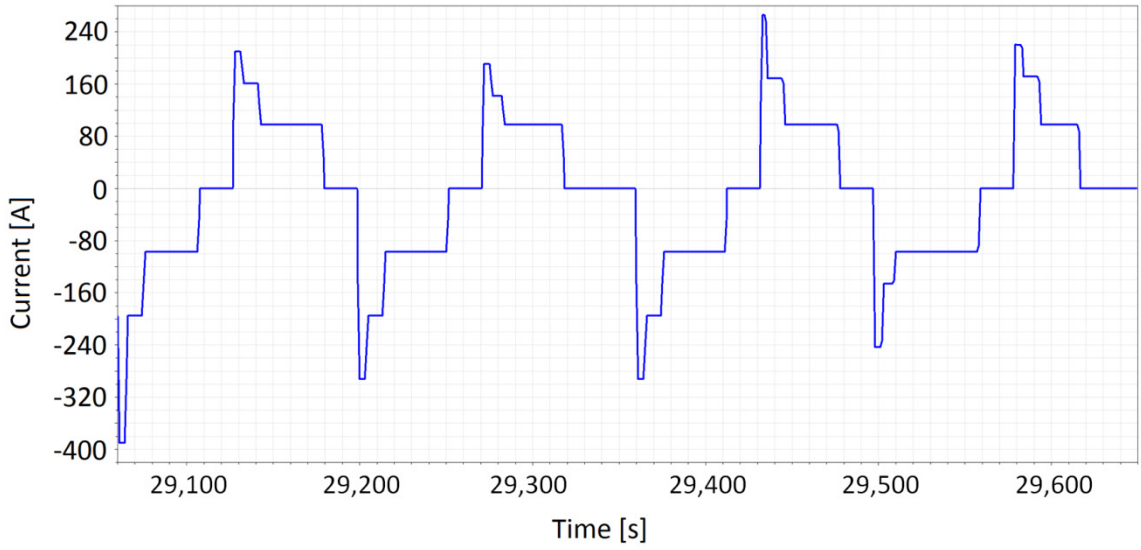

(**a**)

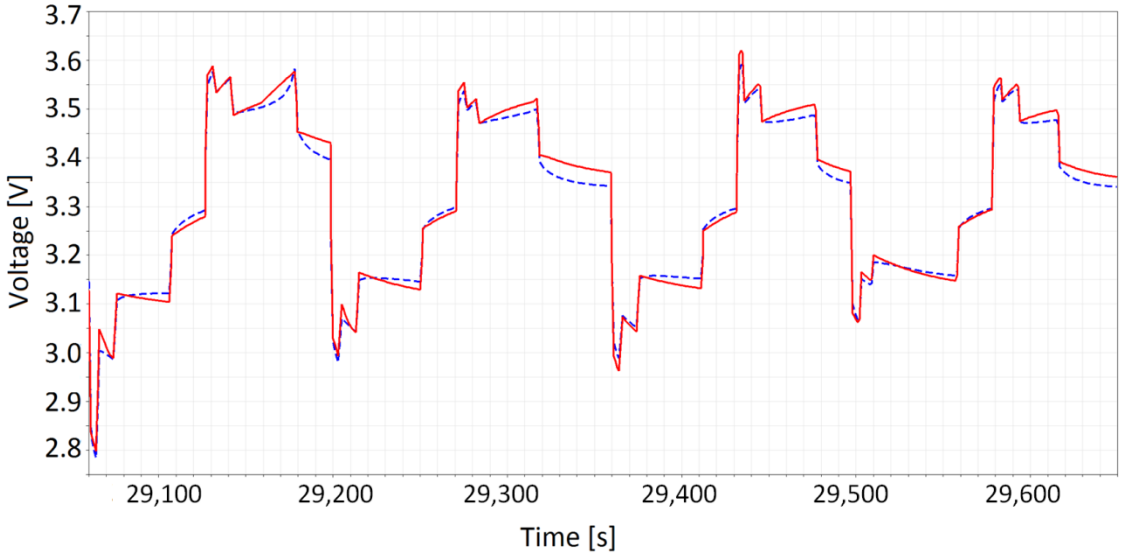

(**b**)

For thermal validation for the LFP cell model, 16 t-type thermocouples were bonded to the cell surface as shown in Figure 8. The thermocouples were fastened using 13 mm × 18 mm labfacility thermopads.

As described previously, the model utilizes an effective temperature when simulating the heat generation and thermal conduction between cells. For the duty-cycle presented in Figure 7a (in the absence of forced air cooling), the observed thermocouple temperatures are shown in Figure 8b. As expected the effective cell temperature should be skewed towards the hottest part of the cell because the electrical current will follow the path of least resistance. This is shown in Figure 8c that compares the temperature logged by thermocouple F7 (c.f., Figure 8a,b) with the effective cell temperature predicted from Equations (8)–(10).

Figure 8. (**a**) Depicting the placement of thermocouples on the LFP 20-A·h pouch cell; (**b**) a plot of temperatures logged by thermocouples placed on an LFP pouch cell as shown in (**a**) under a load cycle depicted in Figure 7a; and (**c**) a comparison of temperature logged by thermocouple F7 and the predicted effective cell temperature.

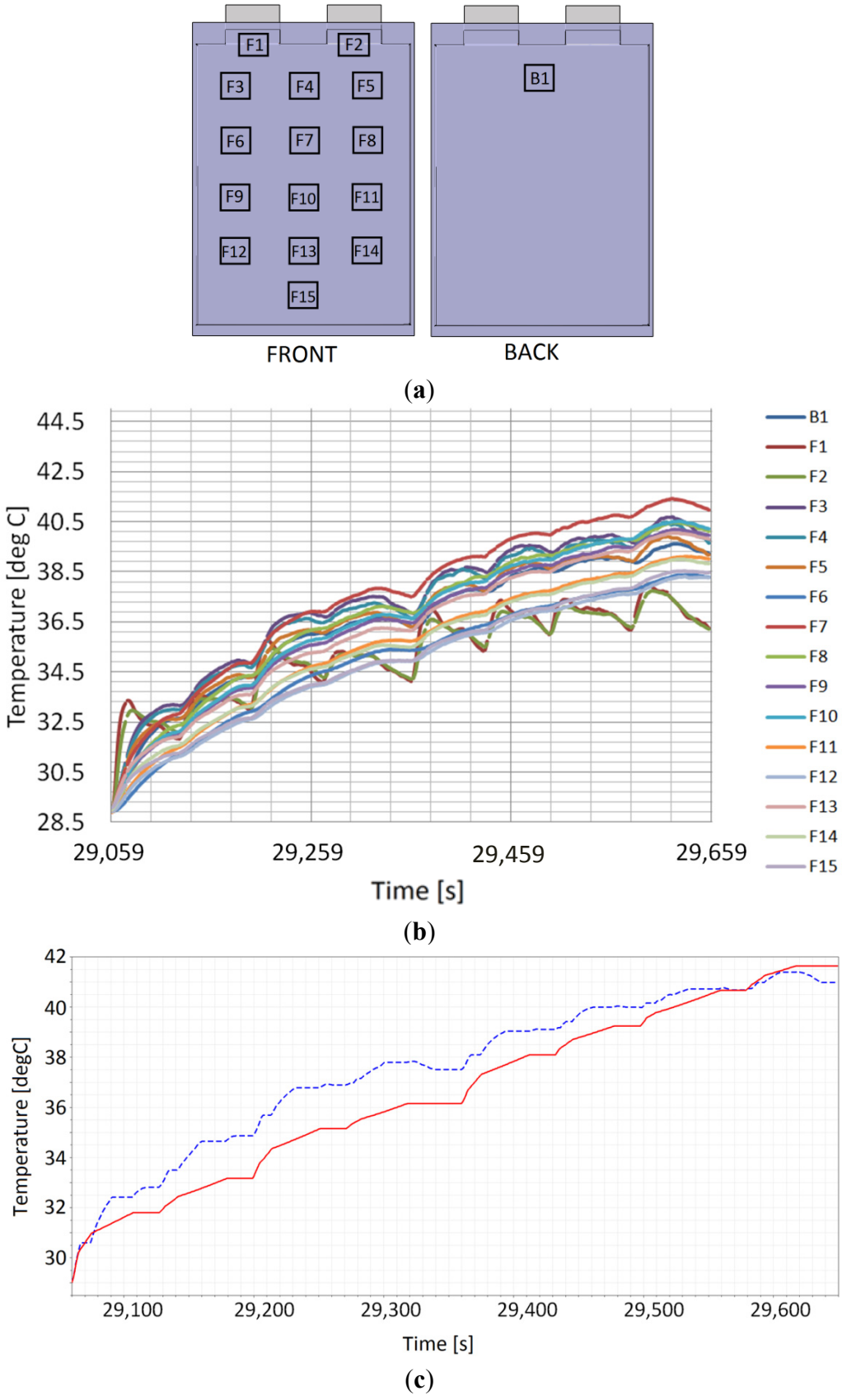

3. Pack Model Development

3.1. Pack Model Structure

3.1.1. Pack Electrical Model

In order to enhance model reusability, the cell model was defined as a Class within the object orientated (OO) simulation environment Dymola. Dymola exploits the OO properties of inheritance and encapsulation in which individual classes can be aggregated hierarchically to facilitate the definition of models that represent both battery modules and complete battery packs. Due to the acsual nature of Dymola, cells within a module may be defined to have either a series or parallel electrical connection; likewise modules can be connected in parallel or series to provide the required electrical characteristics (energy density and power density) for the pack.

Within a real system, cells are physically connected by their tabs; this physical connection is modeled via electrical ports within the class that demands Kirchhoff's law (current and voltage) to be satisfied [28]. At the model definition stage, there is no prescription of inputs and outputs leading to a declarative modeling architecture. As highlighted above, the declarative (acausal) nature of the pack model is an essential feature for model usability and reconfigurability and is the most suitable and consistent way of studying cell-to-cell variations. For example, connecting unbalanced cells in parallel causes current flow; in a procedural or causal context a complex algorithm is required to represent such a phenomenon while in an acausal environment this is straightforward. Further information on this phenomena is provided within [29].

3.1.2. Pack Thermal Model

The definition of the cooling circuit considered consists of cooling plates passing coolant (an incompressible 1:1 mixture of water and ethylene glycol) that is forced by an ideal pump with a mass flow rate m_{flow}. The pressure drop Δp between the pump and the cooling circuit is:

$$\Delta p = \frac{8\zeta}{\pi^2 D^4 \rho} m_{\text{flow}} |m_{\text{flow}}| \tag{17}$$

where D is the diameter of the orifice at the position where ζ is defined; and ζ (assumed to be constant in the turbulent flow regime) is the loss factor with respect to D and ρ is the upstream density. The individual cells are physically connected to the cooling plates; this physical connection is modeled by thermal ports which satisfy generic thermodynamic conservation laws [28]. The cooling model represents a high-level depiction of a generic fluid based cooling system employed within many commercial and prototype EVs and HEVs.

3.2. Pack Model Parameterization

3.2.1. Pack Electrical Model

The electrical model may be characterized, in part, from the battery specifications provided by the cell manufacturer. However, a more robust model definition and parameterization strategy is obtained through the direct characterization of cells using the results from either EIS or HPPC experiments.

Table 1. Statistical analysis of WMG battery laboratory initial characterization of received goods data at 25 °C. Std means standard deviation; MO indicates a mixed oxide electrode cell; P indicates pouch cells; and C indicates cylindrical cells. LMO: manganese spinel; LTO: lithium titanate; and NCA: lithium nickel-cobalt-aluminium oxide.

Cell		LFP (P)	LMO (P)	LTO (P)	NMC_1 (P)	NMC_2 (P)	NMC_3 (P)	MO (P)	NMC_4 (P)	NCA (C)	NMC_5 (P)	NMC_6 (P)
V_{oc}	Std% of mean	0.00%	0.04%	1.11%	7.35%	0.39%	0.06%	5.19%	0.20%	0.13%	0.45%	2.70%
	Range% of mean	0.00%	0.13%	4.17%	23.70%	1.79%	0.27%	17.76%	0.56%	0.83%	1.93%	8.52%
	Std error%	0.00%	0.01%	0.21%	2.25%	0.07%	0.01%	0.92%	0.05%	0.01%	0.10%	0.85%
Impedance 1 kHz	Std% of mean	27.84%	2.05%	3.68%	37.02%	2.93%	2.05%	25.52%	0.00%	1.28%	3.73%	2.13%
	Range% of mean	71.51%	6.58%	15.56%	116.75%	9.69%	9.78%	76.55%	0.00%	7.17%	14.75%	6.24%
	Std error%	5.68%	0.58%	0.68%	10.70%	0.78%	0.32%	4.51%	0.00%	0.06%	0.83%	0.67%
Initial battery capacity	Std% of mean	0.50%	0.05%	1.69%	18.00%	0.51%	0.16%	0.18%	0.00%	0.00%	9.09%	1.63%
	Range% of mean	1.19%	0.09%	3.67%	41.67%	1.34%	0.30%	0.41%	0.00%	0.00%	18.18%	3.16%
	Std error%	0.25%	0.03%	0.84%	9.00%	0.23%	0.09%	0.09%	0.00%	0.00%	5.25%	0.94%
Bus bar resistance	Std% of mean	0.50%	0.50%	0.50%	0.50%	0.50%	0.50%	0.50%	0.50%	0.50%	0.50%	0.50%
	Range% of mean	2.50%	2.50%	2.50%	2.50%	2.50%	2.50%	2.50%	2.50%	2.50%	2.50%	2.50%
	Std error%	0.12%	0.12%	0.12%	0.12%	0.12%	0.12%	0.12%	0.12%	0.12%	0.12%	0.12%

To emulate representative cell-to-cell variations within the overall pack the results discussed in Section 2.2.1 were defined as the nominal or average values for V_{oc}, capacity and impedance.

Further analysis of initial characterization of received goods data (that includes measured data from many hundreds of received cells) is presented in Table 1. A comprehensive understanding of the manufacturing tolerances for each cell facilitates the creation of a stochastic approach to cell parameterization. Each cell within the pack is parameterized using a set of values within the allowable window represented by the statistical mean and the standard deviation (Std). This process is further explained in Figure 9.

Figure 9. (**a**) Dymola model diagram layer showing component array methodology for scalable stacks; and (**b**) Dymola code extract for the cell model class.

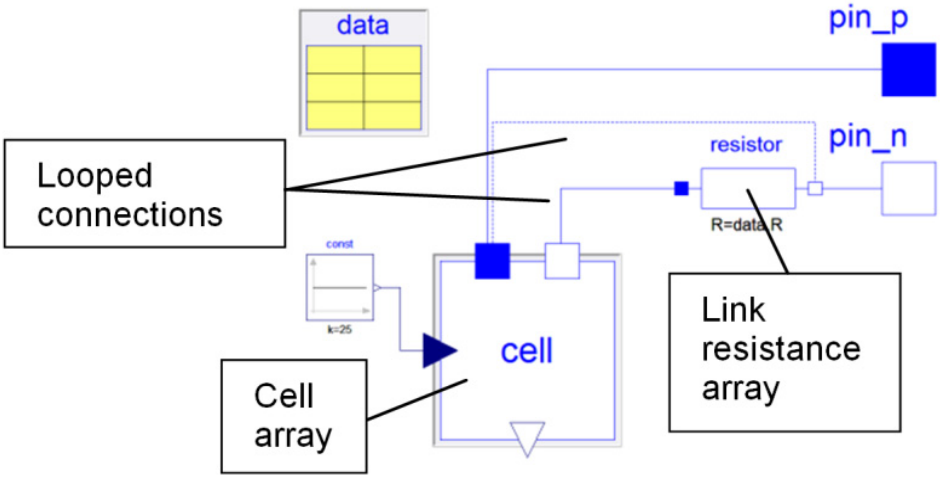

(**a**)

```
connect(pin_p, cell[1].pin_p)

for k in 2:data.n loop
  connect(resistor[k -   1].n, cell[k].pin_p)
end for;

connect(resistor.p, cell.pin_n)
connect(resistor[data.n].n, pin_n)
connect(const.y, cell.Temp)
```

(**b**)

3.2.2. Pack Thermal Model

For the complete battery pack model, the surface area of the cooling plate was taken to be 1.2 m^2, the constant coolant flow rate $m_{\text{flow}} = 27\frac{L}{min}d\frac{8\zeta}{\pi^2 D^4 \rho}$ is taken to be $\ll 1$.

3.3. Model Implementation

A complete physical battery system may exploit a mixture of series and parallel cell configurations to achieve the desired operating voltage and capacity. Since current on a high voltage bus is usually capped by the bus-bar, a large number of cells in series are required to achieve power demand.

This, however, has the disadvantage that a weaker cell can cause an *SOC* imbalance and severe power derating. While using a large number of parallel connected cells can mitigate some of the drawbacks associated with series connections, volume and weight constraints in EVs and HEVs (which will limit the overall number of cells that can be employed) mean that parallel connections will, themselves, not be able to achieve typical power demands. Moreover, an electrical short in a highly parallel system could be challenging because a faulty cell would drain energy from surrounding cells, causing a potentially fire hazard.

To ensure a useable and scalable model architecture, component arrays are employed rather than the instantiation of separate model classes. The advantages of using component arrays over separate instantiations of single components is firstly: less model diagram layer space, but more importantly the ability for the model to be scaled up or down without having to manually redefine the model architecture.

In the example shown in Figure 9a, each element within the cell and resistance arrays (size = n) have been linked using the notation presented in Figure 9b. The Symbolic Manipulator embedded within Dymola is used to simplify the system of equations generated for a model during compilation [28,29,47]. Based on the interconnection of classes, which within the context of the battery system model is cells in series or parallel), the model equations are rearranged into a form where the unknowns variables can be calculated whilst the redundant equations are removed. The simplification of the systems of equations leaves the accuracy of the model intact whilst dramatically reducing the computational effort required to solve the original model equations [29,47,48].

Simulation results and verification of the model are presented within Figure 10. Results are presented for a constant current-constant voltage (CC-CV) charging test on an LFP module comprising of 48 20-A·h cells in a 2p24s configuration (24 serially connected cassettes of two parallelly connected cells). The CC-CV charging regime comprises a charging phase at constant current of 40 A until the battery reaches the manufactures defined cut-off voltage at which point the charging protocol enters a constant voltage phase until 100% *SOC* is achieved. The physical module was cycled and monitored using a Bitrode FTF-500-900 EV/HEV Battery Pack Test System. Thermal measurements were made using 96 t-type thermocouples with an ETAS module and a Campbell data logger. The t-type thermocouples were bonded by the manufacturer using resin.

A commercially available battery system was employed to facilitate validation of a complete battery pack model. The battery system comprises 214 20-A·h LFP cells in a 2p107s configuration. The cells are organized into five modules; four modules with 2p24s configuration and a final module with a 2p11s configuration. There is a manual service interlock within the pack to isolate the complete system for safety into two separate 2p48s and 2p59s modules. The cells are connected via laser welds to the bus bar and the modules are connected via 48 mm^2 copper cables with a measured resistance of 240×10^{-8} Ω and measured inductance of 50 N·h. The pack was cycled and monitored using a Bitrode FTF-500-900 EV/HEV Battery Pack Test System and temperature was recorded using t-type thermocouples connected to a pico-logger configured with a sample rate of 1 Hz. The t-type thermocouples were bonded by the manufacturer using resin. The pack was connected to a cooling system passing liquid coolant at a mass flow-rate of 27 L/min through the cooling plates attached to the bottom of the pack (opposite end to cell tabs).

The pack was cycled with a number of representative plug-in HEV (PHEV) drive-cycles. Figure 11b presents voltage predictions for a pack under a charge sustaining current profile defined in Figure 11a.

The electrical load comprises a 63 min current cycle consisting of three phases; the first 24 min is a charge depleting phase with currents I ranging between −200 A and 130 A, followed by a 34 min phase of constant 40 A charge; the final phase is a second 5 min charge depleting phase with similar current magnitudes defined for first one. As it can be seen from Figure 11b, the maximum discrepancy between modeled and measured voltages was found to be in the order of 28 V (or 0.26 V per cell) during transient discharge. This value represents a peak prediction error of approximately 8% (c.f., Figure 11b). However, it is noteworthy that for the most part of the cycle, in which the battery system is almost in steady-state or under lower transient load, the error is below 7 V (or 66 mV per cell) during transient discharge corresponding to 2%.

Figure 10. (**a**) A comparison of predicted voltage using the cell model (red line) with actual test data (blue line) for the 20-A·h LFP cell; the maximum transient error is less than 0.8 V; (**b**) a comparison of predicted current (red line) with actual test data (dashed blue line) for the 20-A·h LFP cell; and (**c**) a comparison of predicted effective temperature of a single cell (red line) *vs.* maximum recorded temperature and minimum recorded temperature (dashed blue line).

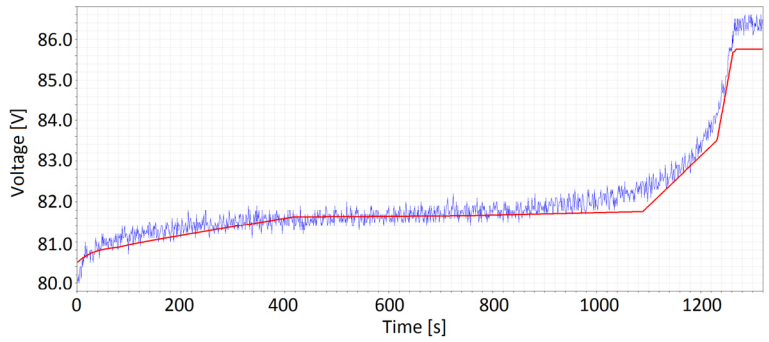

(**a**)

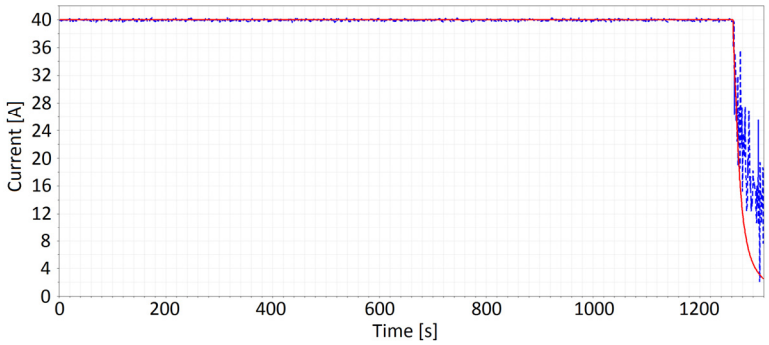

(**b**)

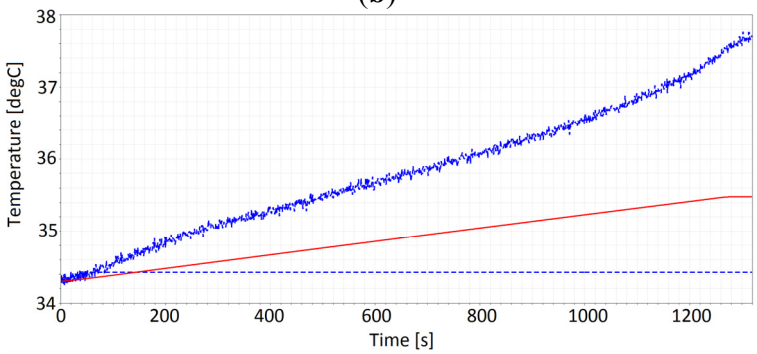

(**c**)

In Figures 10c and 11c, we compare effective cell temperatures with maximum and minimum recorded temperatures within the module and pack respectively. As discussed in Section 2.1.2, the effective temperature represents the homogenous temperature of a theoretically equivalent cell. We find that the effective temperature is not mimicking the hottest part of the module and pack as it did for a single cell, see Figure 8c. This is because the performance of a cell mimics the behavior of the warmer cell when the cells are connected in parallel. When cells are connected in series (as is the case here) the performance is limited by the colder cells. We thus find effective cell temperatures, shown in Figures 10c and 11c, are skewed towards the colder temperatures.

Figure 11. (**a**) Plug-in hybrid electric vehicle (PHEV) current load applied to the 214 20-A·h LFP cell battery pack; (**b**) predicted battery system voltage (red) and measured voltage (blue); and (**c**) compares modeled temperature (solid red line) verses maximum and minimum recorded cell temperature in the pack (dashed blue line).

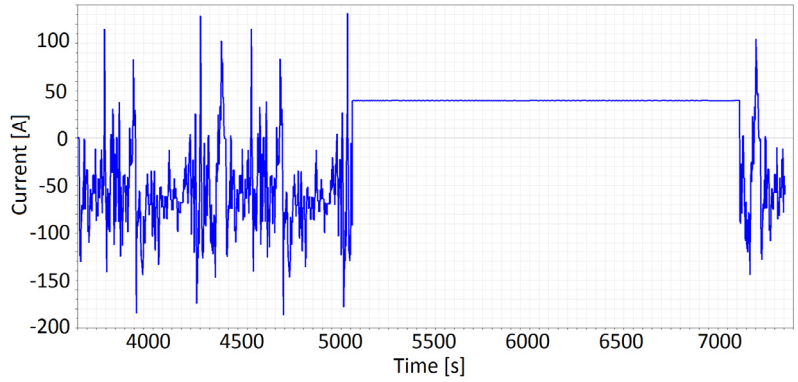

(**a**)

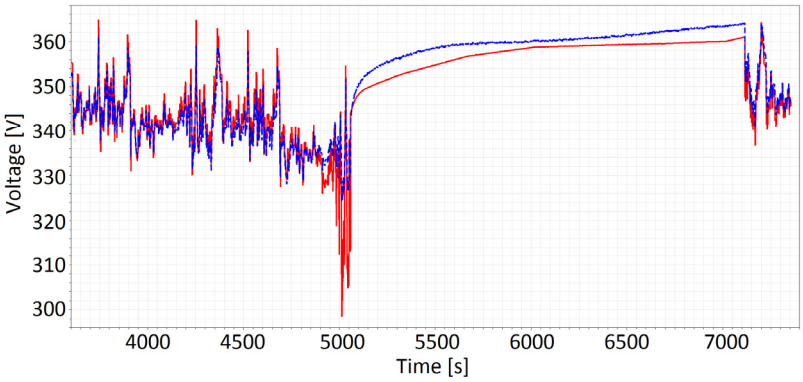

(**b**)

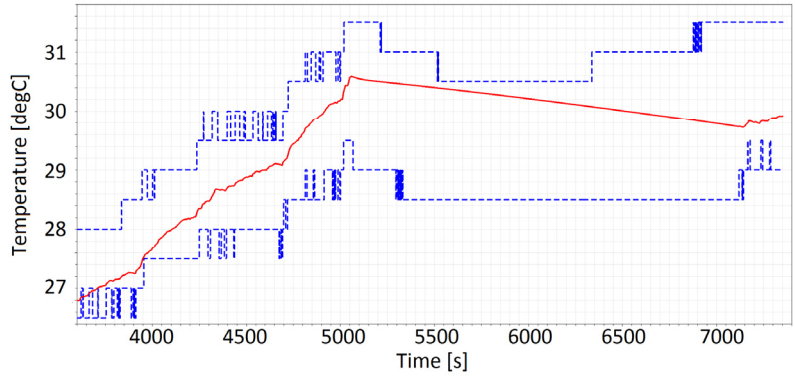

(**c**)

4. Discussion

As highlighted within Figure 12, the simplest approach to account for the impact of diffusion limitation, namely the inclusion of a current dependent RC time constant within the ECM, can lead to small improvements in the voltage prediction capability of the model. In this scenario a time constant is of the form:

$$\tau = R_{\mathrm{d}}\left[2000 + 0.42\left(\int_0^{t_{\mathrm{pulse}}} I_{\mathrm{L}}\mathrm{d}t\right) + 0.012\left(\int_0^{t_{\mathrm{pulse}}} I_{\mathrm{L}}\mathrm{d}t\right)^2\right] \quad (18)$$

Figure 12. Voltage *vs.* time for a 20 A·h LFP cell under a 5C (100 A) discharge pulse for 50 s. Solid line (blue) measured laboratory data; dashed (green) model output with no correction; and dashed-dotted (red) model output that includes a current dependent time constant to emulate diffusion limitation.

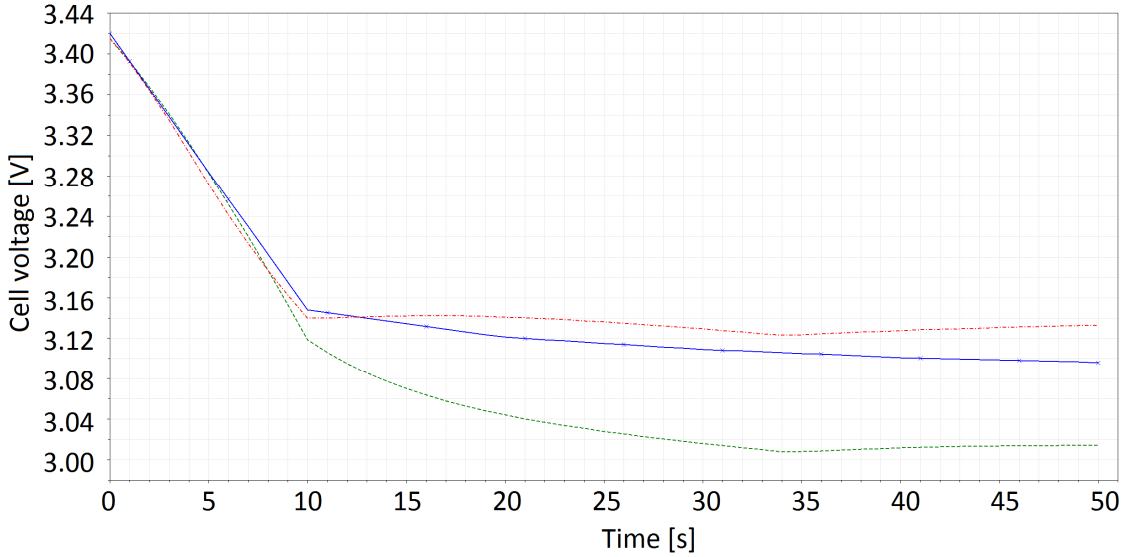

The value of the time constant was derived from experimental HPPC data following the procedure discussed in Section 2.2.1. The authors highlight the challenge of using 10 s pulse data to derive τ. It was found that a suitable prescription to enter and exit the non-linear regime is required to ensure consistent model accuracy.

A fundamental aspect of a representative battery pack model is the inclusion of cell-to-cell variations. As discussed in Section 3, this is readily facilitated by equation based models as opposed to assignment statement based models. A principle advantage of the former is the solution direction of equations will adapt to the data flow context in which the solution is computed. The nature of the equation based approach means that the models are acausal. This in turn means that the model designer is not required to rewrite or rearrange the system equations when using the components in different scenarios, for example forward and inverse dynamic modeling situations or constructing models of different battery system architectures.

The implications of acausality, within the context of studying cell-to-cell variations, are further demonstrated within Figure 13. The results highlight the implications of large $SOC(V_{\mathrm{oc}})$ imbalances within battery packs that contain a large number of parallel connected cells. Initial conditions for the

cells *SOC* were defined within the range of $50 \leq SOC_{\text{initial}} \leq 70$ to an 81p1s 2.2-A·h NMC 18650 module. The unbalanced module was then electrically loaded with a 100-s cycle, comprising 10 10-s saw tooth discharge pulses of around −100 A amplitude followed by 400 s of rest. The Figure shows cells with higher *SOC* are always discharging, as expected, whereas cells with smaller *SOC* are being charged until their V_{oc} exceeds the modules nominal voltage. At the end of cycling the cells in the module act to equilibrate themselves to a common $V_{\text{oc}}(SOC)$.

Figure 13. (**a**) Current (A) *vs.* time (s) for an 81p1s module with randomly assigned initial *SOC* in the range of $50 \leq SOC_{\text{initial}} \leq 70$; and (**b**) *SOC* (%) *vs.* time (s) for an 81p1s module with randomly assigned initial *SOC* in the range of $50 \leq SOC_{\text{initial}} \leq 70$.

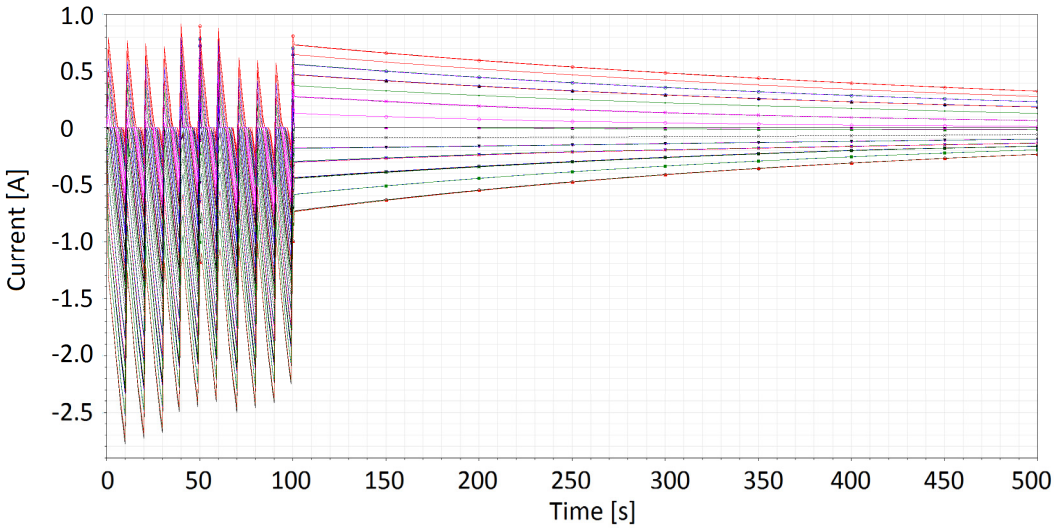

(**a**)

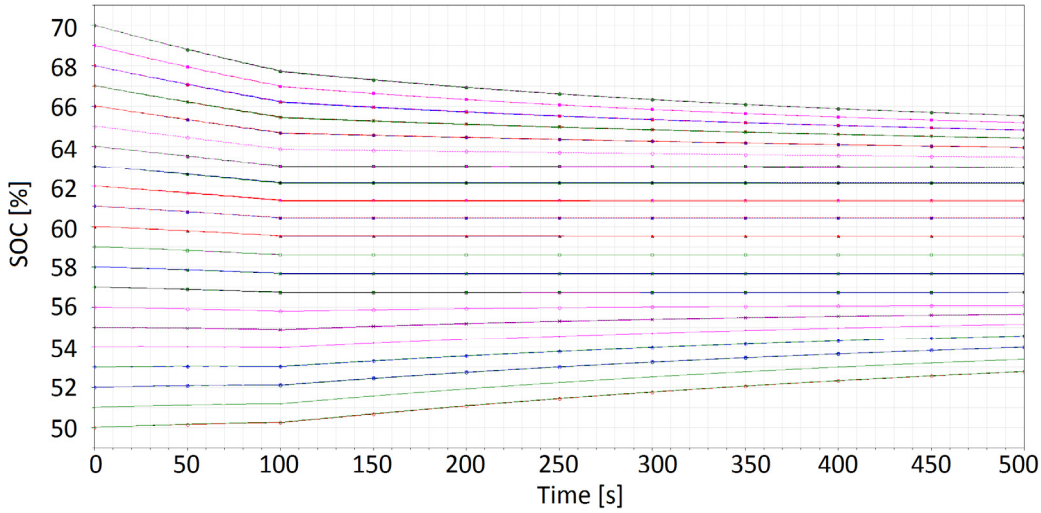

(**b**)

The polarisation and magnitude of individual cell currents within the module depends on the sign and magnitude of the voltage difference: $V_{\text{oc}} - V_{\text{nom}}^{\text{module}}$. Figure 13 shows that cells with higher *SOC* are required to meet pack demands while simultaneously working to re-balance cells with lower *SOC*. It can be seen that, cells with an initial *SOC* of 56% lost capacity during cycling because it's equilibrium voltage was higher than the modules nominal voltage; when the power demand was

switched off the modules nominal voltage immediately rose above the cells V_{oc} resulting in a change of polarity, *i.e.*, causing the cell to then charge towards a module equilibrium. The capacity throughput after 100 s of cells: starting at 70% is 180 A·s, starting at 56% is 17.5 A·s, starting at 50% is 24 A·s. The ability to emulate within a single model structure, the interconnection of cells using both Kirchhoff's voltage law and the current law, is an inherent property of the proposed acausual modeling approach and one that would be prohibitively difficult when using a traditional declaration-based simulation tool.

5. Conclusions

This paper presents the development of an acausal battery model based on an ECM representation of the cell to emulate the electrical dynamics and a coupled, thermal model of the cell. This research extends that previously published, by modifying the circuit elements to take account of both hysteresis and diffusion limitation. The latter is known to be a nonlinear function of large operating currents or prolonged cell operating times.

Validation of the cell model for a number of commercially available cells has been undertaken. Within this paper, detailed validation experiments are presented for both a 30-A·h NMC pouch cell and a 20-A·h LFP pouch cell. The simulation results show that the new model accurately emulates the dynamical characteristics of lithium-ion batteries when exercised under real-world excitation. Exploiting the principles of object orientation and acausal modeling that are available within Dymola, a complete battery pack model is presented based on the inheritance of individual cell models defined as classes. A key attributes of the battery pack model, namely the ability to parameterize the model to represent cell-to-cell variations in V_{oc}, capacity and impedance was demonstrated. The impact of diffusion limitation modelled through a current dependent time constant within the cell model was shown to improve the accuracy of voltage predictions during high current pulses.

Acknowledgments

The research presented within this paper is supported by the UK Technology Strategy Board (TSB) through the WMG Centre High Value Manufacturing (HVM) Catapult in collaboration with Jaguar Land Rover. The authors thank Gael Chouchelamane for assistance in collecting parameterization data. We also thank Widanalage Dhammika Widanage for useful discussions.

Author Contributions

Kotub Uddin proposed the method, developed the model code, analysed the data and wrote the manuscript; Alessandro Picarelli guided the model code development and designed the model user interface; Christopher Lyness advised in aspects of electrochemistry; Nigel Taylor was the technical lead of the Catapult project; and James Marco guided and revised the manuscript.

Nomenclature

A	Cooling plate surface area (m^2)
C_d	Polarization capacitance (F)
C_p	Cell bulk heat capacity (J/(kg·K))

C_{Th}	Transient current load capacitance (F)
D	Diameter of the orifice (m)
G	Cell bulk thermal conductance (W/K)
i (subscript)	i^{th} time-step
I_d	Effective current across the capacitor C_d (A)
I_L	Load current at battery terminals (A)
I_{max}	Maximum manufacturer suggested discharge/charge current of cell (A)
k	Thermal conductivity (W/(m·K))
L	Cell thickness (m)
m	Cell mass (kg)
m_{flow}	Coolant flow rate in pack cooling circuit (L/min)
Δp	Pressure drop between the pump and cooling circuit (psi)
Q	Endothermic heat generated in the cell (J)
Q_{rated}	Battery rated capacity (A·h)
Q_{Th}	Charge accumulated on capacitor C_{Th} (A·h)
R_0	Ohmic resistance (Ω)
R_d	Polarization resistance (Ω)
SOC	State of charge (%)
T	Cell effective temperature (°C)
t_{pulse}	Current pulse length
U_d	Voltage across C_d (V)
U_{oc}	Mean V_{oc} from galvanostatic intermittent titration technique (GITT) experiments (V)
U_{Th}	Voltage across C_{Th} (V)
V_h	Hysteresis voltage (V)
$V_{h,max}$	Maximum hysteresis voltage (V)
V_L	Load voltage at battery terminals (V)
V_{nom}^{module}	Nominal voltage of battery module (V)
V_{oc}	Open circuit voltage (V)
β	Hysteresis voltage capacity (A·h)
ζ	Pressure drop loss factor
τ	Resistor-capacitor (RC) time constant

Conflicts of Interest

The authors declare no conflict of interest.

References

1. Cluzel, C.; Douglas, C. *Cost and Performance of EV Batteries*; Final Report for the Committee on Climate Change; Element Energy Limited: Cambridge, UK, 2012.
2. Tate, E.; Harpster, M.O.; Savagian, P.J. The electrification of the automobile: From conventional hybrid, to plug-in hybrids, to extended-range electric vehicles. In Proceedings of the SAE World Congress & Exhibition, Detroit, MI, USA, 14–17 April 2008; doi:10.4271/2008-01-0458.

3. Franke, T.; Neumann, I.; Bühler, F.; Cocron, P.; Krems, J.F. Experiencing range in an electric vehicle: Understanding psychological barriers. *Appl. Psychol.* **2012**, *61*, 368–391.
4. Nilsson, M. *Electric Vehicles: The Phenomenon of Range Anxiety*; ELVIRE Report; ELVIRE: Babenhausen, Germany, 2011.
5. Meissner, E.; Richter, G. The challenge to the automotive battery industry: The battery has to become an increasingly integrated component within the vehicle electric power system. *J. Power Sources* **2005**, *144*, 438–460.
6. Lu, L.; Han, X.; Li, J.; Hua, J.; Ouyang, M. A review on the key issues for lithium-ion battery management in electric vehicles. *J. Power Sources* **2013**, *226*, 272–288.
7. Fuller, T.F.; Doyle, M.; Newman, J. Relaxation phenomena in lithium-ion-insertion cells. *J. Electrochem. Soc.* **1994**, *141*, 982–990.
8. Srinivasan, V.; Newman, J. Discharge model for the lithium iron-phosphate electrode. *J. Electrochem. Soc.* **2004**, *151*, A1517–A1529.
9. Thorat, I.V.; Joshi, T.; Zaghib, K.; Harb, J.N.; Wheeler, D.R. Understanding rate-limiting mechanisms in $LiFePO_4$ cathodes for Li-ion batteries. *J. Electrochem. Soc.* **2011**, *158*, A1185–A1193.
10. Bazant, M.Z. Theory of chemical kinetics and charge transfer based on nonequilibrium thermodynamics. *Acc. Chem. Res.* **2013**, *46*, 1144–1160.
11. Cogswell, D.A.; Bazant, M.Z. Theory of coherent nucleation in phase-separating nanoparticles. *Nano Lett.* **2013**, *13*, 3036–3041.
12. Bai, P.; Bazant, M.Z. Charge transfer kinetics at the solid-solid interface in porous electrodes. *Nat. Commun.* **2014**, *5*, doi:10.1038/ncomms4585.
13. Feinauer, J.; Spettl, A.; Manke, I.; Strege, S.; Kwade, A.; Pott, A.; Schmidt, V. Structural Characterization of Particle Systems using Spherical Harmonics, 2014. Available online: http://www.mathematik.uni-ulm.de/stochastik/personal/schmidt/publications/SphericalHarmonics.pdf (accessed on 15 July 2014).
14. Subramanian, V.R.; Diwakar, V.D.; Tapriyal, D. Efficient macro-micro scale coupled modeling of batteries. *J. Electrochem. Soc.* **2005**, *152*, A2002–A2008.
15. Subramanian, V.R.; Boovaragavan, V.; Diwakar, V.D. Toward real-time simulation of physics based lithium-ion battery models. *Electrochem. Solid-State Lett.* **2007**, *10*, A255–A260.
16. Bhikkaji, B.; Söderström, T. Reduced order models for diffusion systems. *Int. J. Control* **2001**, *74*, 1543–1557.
17. Dao, T.-S.; Vyasarayani, C.P.; McPhee, J. Simplification and order reduction of lithium-ion battery model based on porous-electrode theory. *J. Power Sources* **2012**, *198*, 329–337.
18. Smith, K.A.; Rahn, C.D.; Wang, C.-Y. Model order reduction of 1D diffusion systems via residue grouping. *J. Dyn. Syst. Meas. Control* **2008**, *130*, doi:10.1115/1.2807068.
19. Cai, L.; White, R.E. Reduction of model order based on proper orthogonal decomposition for lithium-ion battery simulations. *J. Electrochem. Soc.* **2009**, *156*, A154–A161.
20. He, H.; Xiong, R.; Fan, J. Evaluation of lithium-ion battery equivalent circuit models for state of charge estimation by an experimental approach. *Energies* **2011**, *4*, 582–598.
21. Dubarry, M.; Vuillaume, N.; Liaw, B.Y. Origins and accommodation of cell variations in Li-ion battery pack modeling. *Int. J. Energy Res.* **2010**, *34*, 216–231.

22. Dubarry, M.; Vuillaume, N.; Liaw, B.Y. From single cell model to battery pack simulation for Li-ion batteries. *J. Power Sources* **2009**, *186*, 500–507.
23. Wetter, M. Modelica-based modelling and simulation to support research and development in building energy and control systems. *J. Build. Perform. Simul.* **2009**, *2*, 143–161.
24. Surewaard, E.; Tiller, M.; Linzen, D. A comparison of different methods for battery and supercapacitor modeling. In Proceedings of the Future Transportation Technology Conference & Exposition, Costa Mesa, CA, USA, 23–25 June 2003; doi:10.4271/2003-01-2290.
25. Hu, X.; Li, S.; Peng, H. A comparative study of equivalent circuit models for Li-ion batteries. *J. Power Sources* **2012**, *198*, 359–367.
26. Belt, J.R. *Battery Test Manual for Plug-In Hybrid Electric Vehicles*; Idaho National Laboratory: Idaho Falls, ID, USA, 2010.
27. Hu, Y.; Yurkovich, S.; Guezennec, Y.; Yurkovich, B. Electro-thermal battery model identification for automotive applications. *J. Power Sources* **2011**, *196*, 449–457.
28. Fritzson, P. *Principles of Object-Oriented Modeling and Simulation with Modelica 2.1*; John Wiley & Sons: Hoboken, NJ, USA, 2010.
29. Tiller, M. *Introduction to Physical Modeling with Modelica*; Springer: Berlin, Germany, 2001.
30. Hartmann, R.L. An Aging Model for Lithium-Ion Cells. Ph.D. Thesis, The University of Akron, Akron, OH, USA, 2009.
31. Forman, J.C.; Moura, S.J.; Stein, J.L.; Fathy, H.K. Genetic identification and fisher identifiability analysis of the Doyle-Fuller-Newman model from experimental cycling of a $LiFePO_4$ cell. *J. Power Sources* **2012**, *210*, 263–275.
32. Chen, M.; Rincon-Mora, G.A. Accurate electrical battery model capable of predicting runtime and IV performance. *IEEE Trans. Energy Convers.* **2006**, *21*, 504–511.
33. Benini, L.; Castelli, G.; Macii, A.; Macii, E.; Poncino, M.; Scarsi, R. A discrete-time battery model for high-level power estimation. In Proceedings of the Design, Automation and Test in Europe Conference and Exhibition, Paris, France, 27–30 March 2000; pp. 35–39.
34. Lotfi, N.; Fajri, P.; Novosad, S.; Savage, J.; Landers, R.G.; Ferdowsi, M. Development of an experimental testbed for research in lithium-ion battery management systems. *Energies* **2013**, *6*, 5231–5258.
35. Roscher, M.A.; Sauer, D.U. Dynamic electric behavior and open-circuit-voltage modeling of $LiFePO_4$-based lithium ion secondary batteries. *J. Power Sources* **2011**, *196*, 331–336.
36. Newman, J.; Thomas-Alyea, K.E. *Electrochemical Systems*; John Wiley & Sons: Hoboken, NJ, USA, 2012.
37. Smith, K.; Wang, C.-Y. Solid-state diffusion limitations on pulse operation of a lithium ion cell for hybrid electric vehicles. *J. Power Sources* **2006**, *161*, 628–639.
38. Song, L.; Evans, J.W. Electrochemical-thermal model of lithium polymer batteries. *J. Electrochem. Soc.* **2000**, *147*, 2086–2095.
39. Pesaran, A.A. Battery thermal models for hybrid vehicle simulations. *J. Power Sources* **2002**, *110*, 377–382.
40. Troxler, Y.; Wu, B.; Marinescu, M.; Yufit, V.; Patel, Y.; Marquis, A.J.; Brandon, N.P.; Offer, G.J. The effect of thermal gradients on the performance of lithium-ion batteries. *J. Power Sources* **2014**, *247*, 1018–1025.

41. Onda, K.; Kameyama, H.; Hanamoto, T.; Ito, K. Experimental study on heat generation behavior of small lithium-ion secondary batteries. *J. Electrochem. Soc.* **2003**, *150*, A285–A291.
42. Muratori, M. Thermal Characterization of Lithium-Ion Battery Cell. Ph.D. Thesis, Polytechnic University of Milan, Milan, Italy, 2010.
43. Yazami, R.; Reynier, Y. Thermodynamics and crystal structure anomalies in lithium-intercalated graphite. *J. Power Sources* **2006**, *153*, 312–318.
44. Chacko, S.; Chung, Y.M. Thermal modelling of Li-ion polymer battery for electric vehicle drive cycles. *J. Power Sources* **2012**, *213*, 296–303.
45. Bellman, R. *Methods on Nonlinear Analysis*; Elsevier: Amsterdam, The Netherlands, 1970.
46. Horn, Q.C.; White, K. Understanding Lithium-Ion Degradation and Failure Mechanisms by Cross-Section Analysis. In Proceedings of the 211th ECS Meeting, Chicago, IL, USA, 6–10 May 2007; Abstract #318.
47. Broman, D. Meta-Languages and Semantics for Equation-Based Modeling and Simulation. Ph.D. Thesis, Department of Computer and Information Science, Linköping University, Linköpings, Sweden, 2010.
48. Fishwick, P.A. *Handbook of Dynamic System Modeling*; CRC Press: Boca Raton, FL, USA, 2007.